Article:

Kotasidis, FA, Tsoumpas, C, Polycarpou, I et al. (1 more author) (2014) A 5D computational phantom for pharmacokinetic simulation studies in dynamic emission tomography. Computerized Medical Imaging and Graphics, 38 (8). 764 - 773. ISSN 0895-6111

https://doi.org/10.1016/j.compmedimag.2014.06.018

A 5D Computational Phantom for Pharmacokinetic Simulation Studies in Dynamic Emission Tomography

Fotis A. Kotasidis[1,2†], Charalampos Tsoumpas[3,4], Irene Polycarpou[3], Habib Zaidi[1,5,6]

[1]Division of Nuclear Medicine and Molecular Imaging, Geneva University Hospital, Geneva, Switzerland

[2] Wolfson Molecular Imaging Centre, MAHSC, University of Manchester, Manchester, UK

[3]Department of Biomedical Engineering, Division of Imaging Sciences and Biomedical Engineering, King's College London, King's Health Partners, St. Thomas' Hospital, London, UK

[4]Division of Medical Physics, University of Leeds, Leeds, UK[5] Geneva Neuroscience Centre, Geneva University, Geneva, Switzerland

[6]Department of Nuclear Medicine and Molecular Imaging, University of Groningen, University Medical Center Groningen, Groningen, The Netherlands

†Corresponding author:

Fotis Kotasidis, Ph.D
Geneva University Hospital
Division of Nuclear Medicine and Molecular Imaging
CH-1211 Geneva, Switzerland
Tel: +41 22 372 7257
email: fotis.kotasidis@unige.ch

Short running title: 5D computational phantom for dynamic emission tomography

Abstract

Introduction: Dynamic image acquisition protocols are increasingly used in emission tomography for drug development and clinical research. As such, there is a need for computational phantoms to accurately describe both the spatial and temporal distribution of radiotracers, also accounting for periodic and non-periodic physiological processes occurring during data acquisition.

Methods: A new 5D anthropomorphic digital phantom was developed based on a generic simulation platform, for accurate parametric imaging simulation studies in emission tomography. The phantom is based on high spatial and temporal information derived from real 4D MR data and a detailed multi-compartmental pharmacokinetic modelling simulator.

Results: The proposed phantom is comprised of 3 spatial and 2 temporal dimensions, including periodic physiological processes due to respiratory motion and non-periodic functional processes due to tracer kinetics. Example applications are shown in parametric [^{18}F]FDG and [^{15}O]H_2O PET imaging, successfully generating realistic macro- and micro-parametric maps.

Conclusions: The envisaged applications of this digital phantom include the development and evaluation of motion correction and 4D image reconstruction algorithms in PET and SPECT, development of protocols and methods for tracer and drug development as well as new pharmacokinetic parameter estimation algorithms, amongst others. Although the simulation platform is primarily developed for generating dynamic phantoms for emission tomography studies, it can easily be extended to accommodate dynamic MR and CT imaging simulation protocols.

Key words: Parametric imaging, pharmacokinetics, tomography, respiratory motion, phantom, PET, SPECT, MR

I. INTRODUCTION

The continuous development of anthropomorphic and small animal computational phantoms during the last few decades has led to their ever increasing use in clinical and preclinical research [1]. The improved level of their realism and flexibility compared to physical phantoms has led to their widespread use and adoption in emission tomography. The ability to perform simulation studies using these computational phantoms allows a number of methods and techniques used in the field of medical imaging and more specifically emission tomography to be developed, evaluated and validated under controlled and known conditions.

Three-dimensional computational phantoms fall into 3 categories based on their design principle: mathematical stylized phantoms, voxelized phantoms and hybrid equation-voxel phantoms. Mathematical phantoms use mathematical equations to approximate the surface of simple and complex body structures. A number of such designs exist in the literature, such as the Shepp-Logan [2] and the mathematical cardiac-torso (MCAT) phantoms [3]. Such designs are useful, but their inability to model complex structures limits their application, especially since there is need for more realistic simulation studies [4].

On the other hand, voxelized phantoms are based on using segmented anatomical information from high resolution tomographic data (CT or MRI). A number of voxelized phantoms exist, covering anatomical variants (etc...age, sex, body weight and height) [5-9]. Their main advantage is the level of realism compared to stylized approaches; however, fail to provide the level of flexibility offered by mathematical phantoms.

The need to combine the detailed anatomical information provided by voxelized phantoms with the flexibility offered by the mathematical phantoms, has led to the development of hybrid phantoms [10]. These models enable the combination of flexibility and realism within a single anatomical phantom representation. The most popular is the non-uniform rational B-splines (NURBS)-based cardiac-torso (NCAT) phantom [11, 12].

All these three-dimensional (3-D) computational phantoms offer a relatively simple and practical simulation platform, but fail to take into account time-dependent physiological processes occurring during the course of the imaging process. Consequently, this has led to the development of four-dimensional (4D) phantoms incorporating time-dependent processes, such as cardiac and respiratory motion. The NCAT phantom and the latest generation in this family of phantoms, the extended cardiac-torso phantom (XCAT) [13], were generated from multi-detector respiratory-gated CT data, to model cardiac and respiratory motion. Similarly, dynamic MRI has also been used to derive the motion information, which is then used in a four-dimensional (4-D) simulation framework [14, 15].

Although such 4-D phantoms combine accurate anatomical information with models of temporally periodic physiological processes, they do not take into account the variable and temporally non-periodic functional processes occurring during the course of the study, constraining the level of realism and thus their potential application in dynamic studies. However, the need for more accurate quantification both in clinical research and drug development has lead to the increasing use of dynamic imaging protocols [16]. Moreover, pharmacokinetic analysis of the time course of the activity distribution enables more targeted physiological parameters, such as blood flow, metabolism and receptor occupancy, to be derived. In many studies, such parameters are more informative compared to standardized uptake value (SUV) index, which remains the most widely adopted metric in static whole-body PET imaging [17]. Consequently, the development of realistic digital phantoms for multi-compartmental tracer kinetic studies in dynamic PET and SPECT, is of interest. Although a number of studies in the field of image reconstruction and kinetic modelling have used in-house developed parametric phantoms, they often feature roughly approximated anatomical structures with simple geometrical shapes, while lacking the anatomical and physiological variability caused by temporally periodic phenomena such as respiratory motion [18-22]. Recently a variant of the XCAT phantom was developed, named the perfusion cardiac-torso phantom (PCAT), but its scope was limited to dynamic perfusion studies in cardiac imaging [23].

In this work, using high resolution anatomical and temporal information from real MR data, we develop a five-dimensional (5-D) computational anthropomorphic phantom, incorporating temporal gating from respiratory induced body motion and compartmental modelling tracer kinetic capabilities for parametric imaging simulation studies in dynamic emission tomography. This new voxelized phantom, allows respiratory gated and non-gated datasets to be simulated along with any tracer-specific compartmental model representing the temporal distribution of the activity concentration during dynamic imaging protocols in PET and SPECT. Rather than being region and application specific, kinetic parameters are freely assigned in the entire field-of-view (FOV), generating voxel-wise parametric maps based on the tracer of interest.

II. METHODS

This Section describes the generic methodology used by the simulation platform for generating 5D parametric imaging simulation phantoms using MR information for discerning anatomy and motion along with a kinetic modelling simulator and a virtual tomograph.

THE KCL-HUG SERIES 5-D PHANTOM

1. 3D Anatomical Phantom

Anatomical information are obtained from a high resolution 3D MRI scan and different organ structures are segmented in order to generate the anatomical regions comprising the phantom, as described in Tsoumpas *et al.* [24] and Buerger *et al.* [25]. Segmentation of the major structures is performed using a semi-automatic algorithm with local thresholding [25]. This allows fast generation of 3D anatomical phantoms, facilitating personalized patient-specific anatomical phantom designs, derived from a real MR scan. Apart from template organ structures segmented from the MRI data, tumors of varying characteristics (e.g size and tracer uptake) can be manually inserted in different phantom regions. However, since these tumors represent additional patient-specific structural variants, they can easily be manipulated. Other anatomical variants can also be included depending on the required anatomy and simulation conditions. Tumours or other anatomical variants can be manually delineated/drawn on the 3D anatomical phantom and the tumor ROI mask can be saved and given a separate value, different to the region it is embedded within. The complete anatomical phantom is a superposition of separate regions segmented from the MRI data.

2. 4D Dynamic Phantom For 1-Tissue and 2-Tissue Models

To describe the temporal distribution of a given tracer and simulate time-activity curves (TACs), custom-made software capable of providing multi-compartmental modelling for 1-tissue and 2-tissue models, was developed. Given an input function, a temporal sampling protocol and known tracer-specific pharmacokinetic parameters (constant rates) controlling the bi-direction flux of the tracer between the blood and tissue compartments (for each organ structure in the anatomical phantom), TACs are generated. Typical input functions derived from arterial sampling can be used, along with user defined ones, based on a parameterized model. For the sampling protocol, any number of frames and frame durations can be accommodated within the typical scan times used for dynamic studies in emission tomography. A blood volume component can also be included to generate the simulated TACs, since typically both tissue and blood components are sampled at the voxel level in clinical acquisitions. The same principles apply for the different kinetic parameters used, with separate constant rates for the different organs and values obtained from the literature, if a generic activity distribution is to be realized. Alternatively, if a dynamic emission scan is available from a patient, personalized patient-specific pharmacokinetic parameters can be used based on mean organ parameters. Although individual micro-parameters are the endpoint parameters of interest, in

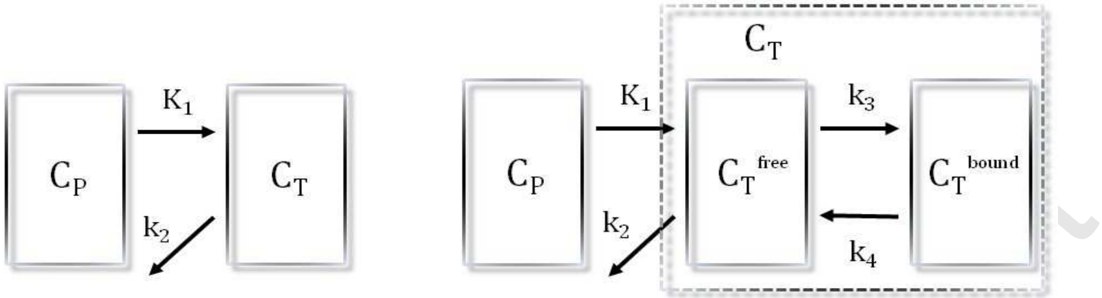

Fig. 1. Schematic diagram of a single-tissue and a two-tissue kinetic model showing the different compartments as well as the constant rate controlling the rate of change in activity concentration for each compartment.

some applications certain macro-parameters, such as the volume of distribution (V_T) and the tracer's net uptake rate into the irreversibly bound compartment (K_i) are often more relevant and provide a more complete picture of the underlying patho-physiology. These macro-parameters are combinations of micro-parameters and can easily be adjusted to reflect specific conditions. Generic schematic diagrams for a single-tissue and a two-tissue compartment model, used to generate the dynamic phantom image sequence, are shown in Fig. 1. The time-dependent activity concentration in the tissue C_T, can be described as a convolution of the impulse response function (IRF), which is the response of the system to a delta-function, with the time-dependent activity concentration in the plasma Cp. For the single-tissue model, the time-course of the activity distribution can be described as:

$$C_T = IRF(K_1, k_2, t) \otimes C_P = K_1 e^{-k_2 t} \otimes C_p = K_1 e^{-\left(K_1 / V_T \right) t} \otimes C_p \qquad (1)$$

where K_1 is the plasma to tissue rate constant (*ml/s/ml*). K_1 can be further parameterized, based on the Renkin-Crone model, as a product of blood flow (perfusion) and extraction fraction as

$$K_1 = EF = \left(1 - e^{-\left(PS / F \right)} \right) F \qquad (2)$$

where *PS* is the permeability surface area product, *E* is the extraction fraction and *F* is the blood flow [26, 27]. For tracers with high permeability surface area product, extraction is close to unity and is independent of flow and therefore K_1 provides a measure of blood flow [28]. The platform is highly flexible, enabling to define the plasma-to-tissue influx rate by adjusting the permeability surface product and subsequently the extraction fraction, based

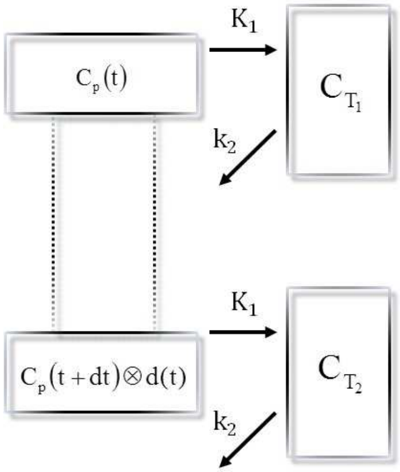

Fig. 2. Schematic diagram of a single-tissue model at 2 different target regions. As the injected bolus passes through the blood stream it becomes dispersed while its arrival time is shifted.

on the selected tracer. Alternatively, one can directly assign a fixed value for K_1. Similarly, k_2 can be given directly or as a ratio of the influx rate (K_1) and volume of distribution (V_T).

For the two-tissue model, the time-course of the activity distribution can be described as:

$$C_T = IRF(K_1,k_2,k_3,k_4,t)\otimes C_P = \frac{K_1}{(a_2-a_1)}\left[(k_3+k_4-a_1)e^{-a_1t}+(a_2-k_3-k_4)e^{-a_2t}\right]\otimes C_P \qquad (3)$$

where $$a_1 = \frac{(k_2+k_3+k_4)-\sqrt{(k_2+k_3+k_4)^2-4k_2k_4}}{2} \qquad (4)$$

and $$a_2 = \frac{(k_2+k_3+k_4)+\sqrt{(k_2+k_3+k_4)^2-4k_2k_4}}{2} \qquad (5)$$

Simple or complex models can be realized in different organs, including dual input function models simulating both arterial and venous blood supply in certain organs such as the liver [29]. Furthermore, the differential temporal distribution of the activity concentration in the blood as it circulates through the blood vessels, can be taken into account, with differential delay and dispersion in the input function in adjacent regions (Fig. 2) [30]:

$$C_P{}'(t) = C_P(t - \Delta t) + \tau \frac{dC_P(t - \Delta t)}{dt} \tag{6}$$

Given an input function *Cp(t)*, a delay (Δt) and a dispersion coefficient (τ) one can estimate *Cp'(t)*. The tracer's radioactive decay can also be taken into account and incorporated into the operational equations as a global parameter.

TACs are assigned at the voxel level, generating time series of voxelized phantoms (4D phantom) with a temporal sampling dictated by the dynamic acquisition protocol selected during the TAC generation. Although only the case for single- and two-tissue models is presented in this work, the simulation platform allows any kinetic model variant to be accommodated with an increasing degree of complexity and is therefore applicable for simulating kinetics for any tracer and protocol.

3. 5D Phantom Using MR-Derived Motion Fields

So far the 4D phantom corresponds to a single reference position without including any information regarding respiratory motion. To simulate different types of realistic motion during a dynamic scan, the fast analytic simulation toolkit (FAST) is used [15]. A dynamic 4D MRI scan, providing uniform temporal sampling over consecutive respiratory cycles during the dynamic scan, is used to generate the motion fields. This is achieved using the amplitude signal from a virtual navigator and selecting a number of dynamic images from different phases of the respiratory cycle as the respiratory gates. A reference gate is then selected with the remaining gates being registered to the reference gate, in order to generate the motion fields. These MR-generated motion fields are subsequently used to warp the dynamic phantom emission data and generate a number of respiratory gates for each time frame in the dynamic image sequence. Using this methodology, deep and shallow breathing can be simulated along with other non-periodic types of motion. If anatomical variants, such as tumors, are utilized in the phantom, motion is simulated similar to the rest of the regions. Therefore, the tumor's shape (along with the other regions) is deformed based on the motion fields, and as such, the deformation depends on where the tumor is located.

4. 5D Projection Data

The simulated gated dynamic emission and attenuation data can then be used in conjunction with any medical imaging simulation package which models the physics, image acquisition and detector properties of medical imaging systems. Data can be forward projected to generate projection datasets for investigation of numerous methods and techniques for motion correction, image reconstruction, and kinetic parameter estimation.

III. APPLICATION IN METABOLIC AND BLOOD FLOW PET PARAMETRIC IMAGING

In order to evaluate the phantom design and demonstrate the potential application of this simulation platform in drug, clinical, algorithmic and methodology development, different clinical protocols were realized. Two dynamic PET protocols corresponding to a metabolic imaging study with [^{18}F]FDG and a perfusion study with [^{15}O]H_2O were simulated and reconstructed. Subsequently and following image reconstruction, full kinetic analysis was performed on the dynamic datasets and parametric maps of micro- and macro-parameters were generated.

1. 3D Anatomical Phantom

To generate the anatomical phantom, high resolution anatomical information (2×2×2 mm^3), covering the thoracic and upper abdominal area have been obtained from a healthy volunteer using MRI data [25]. As cortical bone is not normally visible using common MR sequences, an ultra-short echo-time (UTE) 3D MRI sequence was acquired (TR 6.5ms, flip angle 10^o) obtaining one image during the free induction decay (TE_1=0.14ms) and one during the first echo time (TE_2=4.6ms). Data were respiratory corrected to the end-exhale position. From the difference image between the 2 UTE images, a number of regions of interest were segmented (soft tissue, cortical bones, liver and lungs) and used to construct the anatomical phantom. The myocardium, heart ventricles and large vessels were also segmented using a different ECG triggered balanced B-TFE MRI scan during free breathing (TR/TE 4.7 ms/2.36 ms, TFE factor 26, flip angle of 90^o) [15, 31]. The scan was subsequently respiratory gated again to the end-exhale position using a virtual navigator. Based on these 2 MRI scans, the different segmented regions were combined to generate the anatomical phantom. Nine tumors of varying size were also embedded in the lung (3), liver (3) and dome of the diaphragm (3). The tumors were drawn on the phantom and the tumor masks were inserted as separate regions. The anatomical phantom was then sub-sampled to a volumetric resolution of 2×2×2mm^3 in order to represent typical voxel resolution encountered in PET imaging, with an image volume of 336×336×81 voxels. Based on the segmented organs that were used to generate the anatomical phantom, an attenuation map was also generated using a 4-region classification of the phantom.(air: 0 cm^{-1}, lung: 0.03 cm^{-1}, soft tissue: 0.099 cm^{-1}, and bone: 0.15 cm^{-1}).

2. 4D Dynamic Phantom For [^{15}O]H_2O and [^{18}F]FDG Models

Two dynamic PET protocols were simulated, corresponding to typical [^{15}O]H_2O and [^{18}F]FDG scanning sessions and representing a single-tissue and a two-tissue model. For the [^{15}O]H_2O protocol, TACs were generated using a single-tissue 3 parameter model, including a blood volume component (K_1, k_2, bv). A 360 seconds total scan duration was selected binned into 28 non-uniformly sampled time frames [14×5 s, 5×10 s, 3×20 s, 6×30 s], representing a typical [^{15}O]H_2O protocol [32]:

$$C_T = IRF(K_1, k_2, t) \otimes C_P + bvC_p = K_1 e^{-k_2 t} \otimes C_p + bvC_p \tag{7}$$

For the [^{18}F]FDG protocol, TACs were generated using a two-tissue 4 parameter model assuming irreversible kinetics during the course of the scan (k_4=0) and including also a blood volume component (K_1, k_2, k_3 and bv). A 3300 seconds total scan duration was chosen binned into 29 non-uniformly sampled time frames [9×10 s, 3×30 s, 4×60 s, 4×120 s, 8×300 s] [33]:

$$C_T = IRF(K_1, k_2, k_3, t) \otimes C_P + bvC_p = K_1\left(e^{-(k_2+k_3)t} + \frac{k_3}{(k_3+k_2)}\left(1 - e^{-(k_2+k_3)t}\right)\right) \otimes C_p + bvC_p \tag{8}$$

In both imaging protocols, a single input function model was used, representing delivery through arterial blood, while no differential delay and dispersion were used in simulating the kinetics for the different regions, with a common reference delivery time between them. Furthermore, kinetic parameters derived from the literature, summarized in Tables I and II, were used to generate the dynamic data. For the [^{15}O]H_2O study, a measured input function was used while for the [^{18}F]FDG data a population based input function was used.

TABLE I. Simulated kinetic parameters for the single-tissue model.

	K_1 ml/s/ml	k_2 ml/s/ml	Bv ml/ml	V_T ml/ml
Lungs	0.0008	0.0014	0.06	0.6
Bone	0.0018	0.0027	0.00	0.69
Soft tissue	0.0005	0.0042	0.00	0.12
Ventricles	0.0000	0.0000	1.00	0.00
Myocardium	0.0167	0.0183	0.15	0.91
Tumors	0.0098	0.0161	0.08	0.61
Liver	0.0117	0.0119	0.05	0.98

TABLE II. Simulated kinetic parameters for the two-tissue model.

	K_1 ml/s/ml	k_2 ml/s/ml	k_3 ml/s/ml	Bv ml/ml	K_i ml/s/ml
Lungs	0.0007	0.0048	0.0006	0.1510	0.0001
Bone	0.0027	0.0033	0.0010	0.0000	0.0006
Soft tissue	0.0008	0.0054	0.0014	0.0190	0.0002
Ventricles	0.0000	0.0000	0.0000	1.0000	0.0000
Myocardium	0.0033	0.0170	0.0025	0.5450	0.0004
Tumors	0.0031	0.0073	0.0056	0.0800	0.0014
Liver	0.0209	0.0222	0.0000	0.1650	0.0000

3. Respiratory Data

4D MR data were also acquired from the same healthy volunteer, providing a uniform temporal sampling of a few complete respiratory cycles (~25 seconds dynamic acquisition with 0.7 seconds temporal sampling - 35 dynamic image volumes) as described by Buerger *et al* [25]. An amplitude signal from a virtual navigator on the diaphragm dome was then generated and 8 dynamic images were chosen to sample a full respiratory cycle. Subsequently, each gated image, corresponding to a different phase in the respiratory cycle, was registered to the reference gate (i.e. end-exhale position) to estimate the corresponding motion fields, using a local affine registration algorithm [34]. Using the MRI-derived motion fields, the dynamic emission phantom images were warped into 8 different phases over the respiratory cycle, representing a shallow breathing pattern. Therefore, 8 gated 3-D images were generated for each time frame in the dynamic 4D phantom (3 spatial dimensions {336 × 336 × 81} × 28/29 time frames × 8 respiratory gates). Attenuation data were treated similarly, generating 8 gated attenuation maps for each phase in the respiratory cycle, but using the same gated maps for all the time frames since no motion between the kinetic modelling time frames was taken into account in this study (3 spatial dimensions {336 × 336 × 81} × 8 respiratory gates).

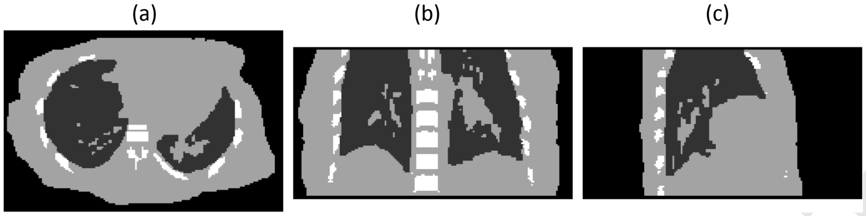

Fig. 3. Transverse (a), coronal (b) and sagittal (c) images of the simulated attenuation map corresponding to a single gate.

4. 5D Projection Data

To generate the forward projected data, an in-house simulator was used. The dynamic emission images for each respiratory gate and time frame along with the respiratory gated attenuation images, were forward projected into a virtual scanner using Siddon's line of response driven algorithm, along with the geometry configuration of the Biograph 6 Barrel HiRez PET/CT scanner (Siemens Molecular Imaging Inc.TN, USA) [35]. Both the noiseless emission as well as attenuation projection data were histogrammed into a 336 × 336 × 313 3-D sinogram (336 × 336 × 313 × 28/29 time frames × 8 respiratory gates for the emission data and 336 × 336 × 313 × 8 respiratory gates for the attenuation data). Subsequently the emission projection data were attenuated to generate the attenuated emission sinogram for each respiratory gate and time frame.

5. Image Reconstruction and Kinetic Modelling

The generated projection data were reconstructed using in-house developed image reconstruction software capable of reconstructing data from the Biograph 6 HiRez PET/CT [36]. Data from were reconstructed using an ordinary Poisson ordered subsets expectation maximization algorithm (OP-OSEM) with 10 iterations (21 subsets). Following image reconstruction, full compartmental analysis of the dynamic datasets was performed to derive parametric maps of micro- and macro-parameters of interests. For both clinical datasets, kinetic modelling equations similar to those used to generate the data, were used to model the time-course of the activity distribution. The models were linearized using the generalized linear least square (GLLS) method [37, 38], and model parameters were fitted to the measured data by minimizing a non-negative weighted least square objective function (NNWLS). For the [^{15}O]H$_2$O dataset, the GLLS was used with 2 internal iterations while parameter initialization was based on the linear least square algorithm (LLS) [37]. For the [^{18}F]FDG dataset, 4 internal GLLS

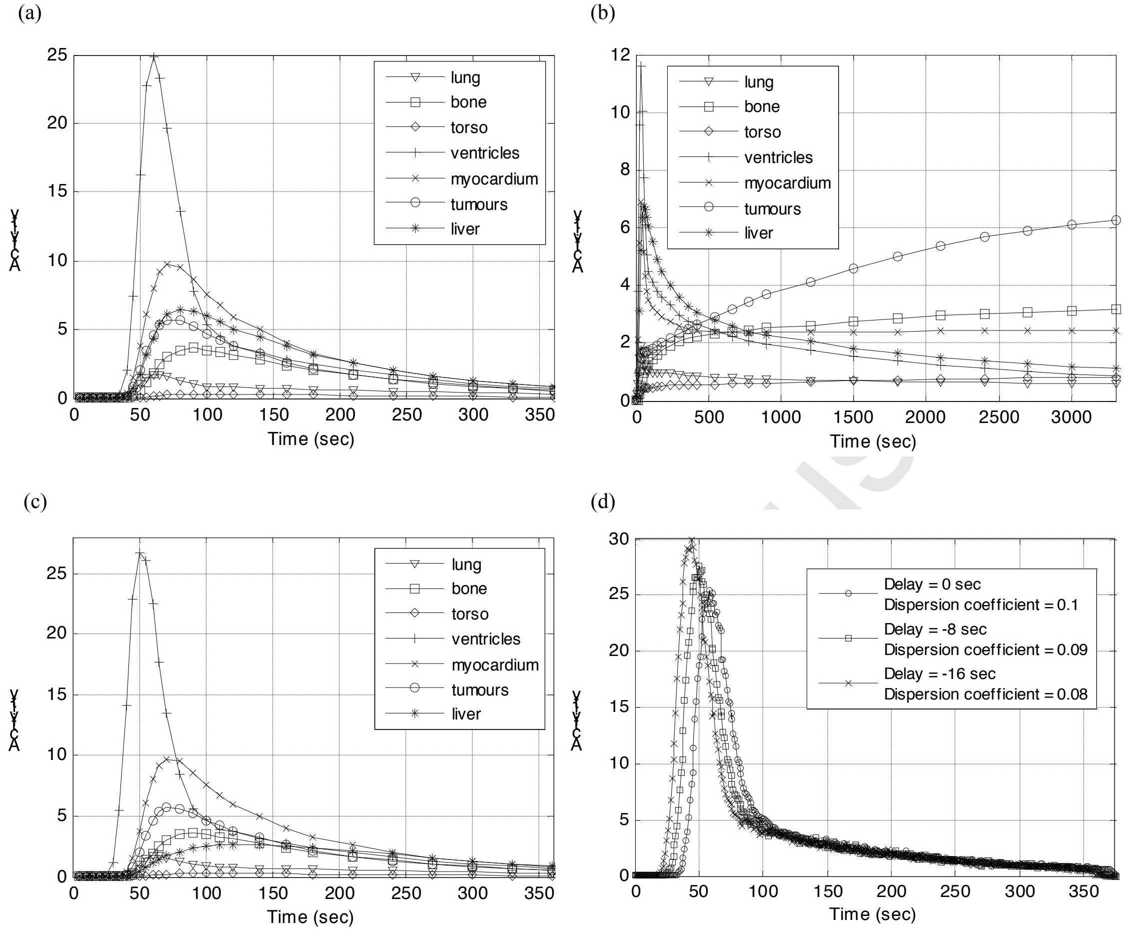

Fig. 4. Simulated TACs representing (a) [^{15}O]H_2O and (b) [^{18}F]FDG kinetics, used for the different regions in the 3D anatomical phantom. Input functions with differential delay and dispersion in different organs can be used while organ TACs having a dual input function delivery can also be simulated. The simulated [^{15}O]H_2O TACs from (a) are shown in (c) using a dual input model in the liver, while 3 input functions from a [^{15}O]H_2O scan with different delay and dispersion are shown in (d).

iterations were used, while initialization was based on uniform parameters. For the [^{15}O]H_2O data, parametric images of perfusion (K_1), clearance rate (k_2), fractional blood volume (bv) and volume of distribution (V_T), were derived. Similar for the [^{18}F]FDG data, parametric images of K_1, k_2, k_3, bv and net uptake rate $K_{i.}$ were generated.

IV. RESULTS

Six regions were segmented from the 3D MRI scans: soft tissue, liver, heart ventricles, lungs, rib cage and spine and myocardium. Representative slices through the simulated attenuation map of the combined anthropomorphic phantom are shown in Fig. 3. Using the kinetic parameters from Tables I and II and the kinetic modelling operational equations, TACs for each organ region were generated and plotted in Fig.4. In Fig. 4(a), the generated TACs from the [^{15}O]H_2O study are shown for all 6 regions as well as the embedded tumors. Regions with high K_1

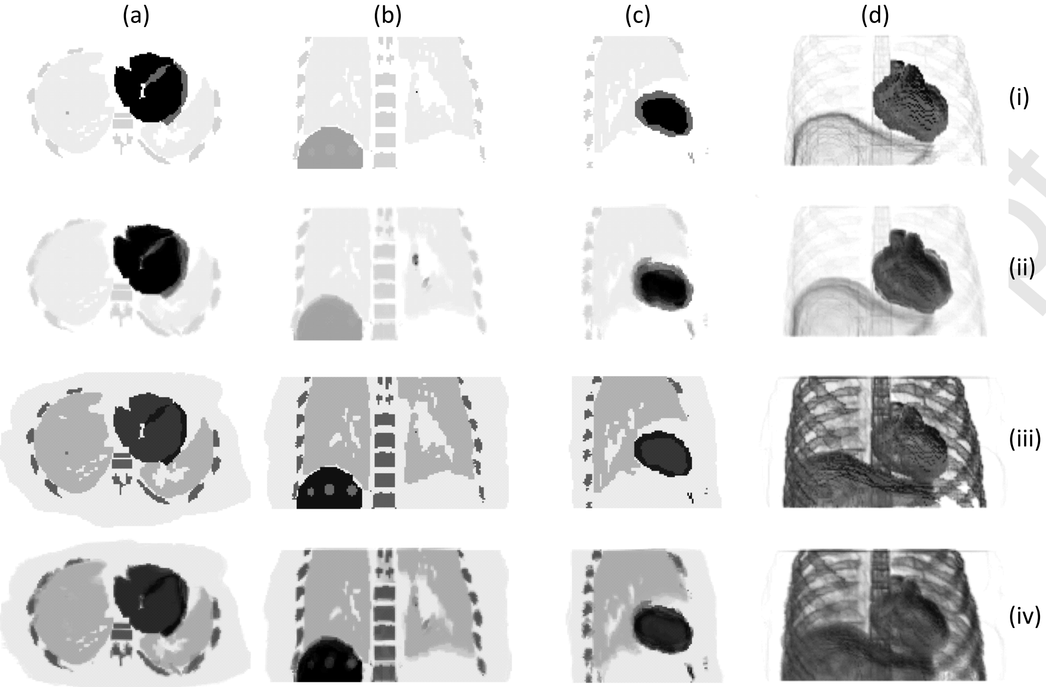

Fig. 5. Transverse (a), coronal (b), sagittal (c) and 3D rendered (d) simulated images of the [^{15}O]H_2O phantom at 2 different time points during the simulated dynamic [^{15}O]H_2O image sequence corresponding to an early time frame (i-ii) (t = t_0 +20 s) and a late time frame (iii-iv) (t = t_0 +360 s) where t_0 is the reference start time. Images are shown for a single respiratory gate (i, iii) and for all gates superimposed (ii, iv).

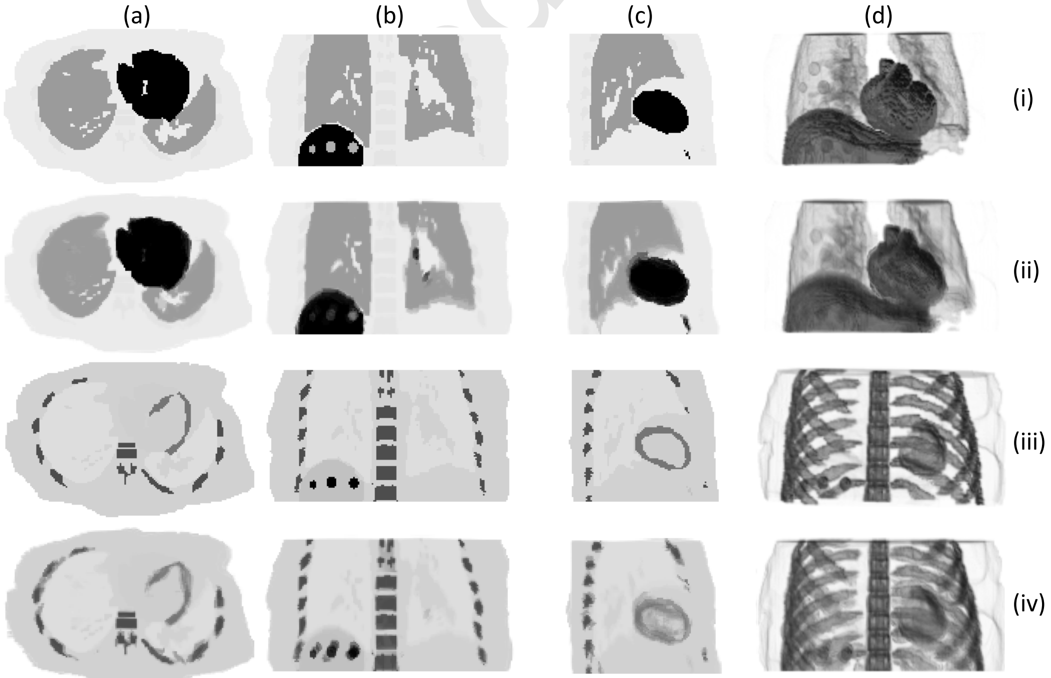

Fig. 6. Transverse (a), coronal (b), sagittal (c) and 3D rendered (d) simulated images of the [^{18}F]FDG phantom at 2 different time points during the simulated dynamic [^{18}F]FDG image sequence corresponding to an early time frame (i-ii) (t = t_0 +40 s) and a late time frame (iii-iv) (t = t_0 +3400 s) where t_0 is the reference start time. Images are shown for a single respiratory gate (i, iii) and for all gates superimposed (ii, iv).

such as the myocardium and the tumors exhibit a high upslope, with the washout of the tracer governed by $k_{2.}$ Similarly, Fig. 4(c) shows the same TACs but using a dual input function model in the liver while in the rest of the regions, a single arterial input function model is used, similar to the one used in Fig.4(a). The dual input model in the liver, represents tracer delivery from both the hepatic artery and portal vein. In order to simulate the portal vein, the gastrointestinal compartment can be used, representing a region outside the simulated patient's FOV, which is a single compartment model between the arterial blood and the gut compartment. Although a delay in the delivery of each input can also be accommodated, no delay between the arterial and portal input functions was assumed. The TAC in the heart ventricles which represents the activity concentration in the arterial blood, was simulated using a blood volume component equal to unity as can be seen from Table 1, with no contribution from the tissue component. Hence, the TAC is equal to the input function. To simulate the more realistic case of differential tracer delivery time in different regions, including differential dispersion of the input function, the generated TACs in each region can take these effects into account. Three input functions are shown in Fig. 4d with 8 second delay between them and different dispersion coefficients. By changing the delay, the input function is shifted with respect to the reference global zero time point in the simulated protocol. Simulated TACs for the [^{18}F]FDG dataset are shown in Fig. 4b, again for the same regions. Looking at the tumor TAC, the trapping of the tracer is evident due to the irreversible kinetics attributed to a high simulated k_3 parameter and a $k_4 = 0$ which is a valid assumption for the duration of a typical [^{18}F]FDG scan. Similar to the [^{15}O]H_2O dataset shown in Fig. 4a, the activity concentration in the ventricles is representative of the input function. The simulated TACs shown in Figs. 4a and 4b were used to generate the dynamic phantoms for the [^{15}O]H_2O and [^{18}F]FDG studies.

Representative emission data from the simulated dynamic and respiratory gated [^{15}O]H_2O and [^{18}F]FDG phantoms are shown in Figs. 5 and 6, respectively. Fig. 5 shows typical slices and volume rendered images from early and late time frames into the dynamic [^{15}O]H_2O dataset. The images are shown for a single respiratory gated phase (one of the 8 gated images), which corresponds to the reference gate (end-exhale position). In the early frame, activity is high in the heart ventricles and aorta, representing the input function as seen in Fig. 4, with the tissue response governed by the influx rate constant. Conversely, in the late frame, activity is representative of the tracer's washout. As the temporal frames are shown from a single gate position, they correspond effectively to motionless data and hence without any blurring in the voxelized dynamic data. The same time frames are shown in Fig. 5 (ii) and (iv) but with all 8 respiratory gated images superimposed, creating a blurred representation of the simulated activity distribution. Although 8 gates were simulated in this study, different gates can be included or

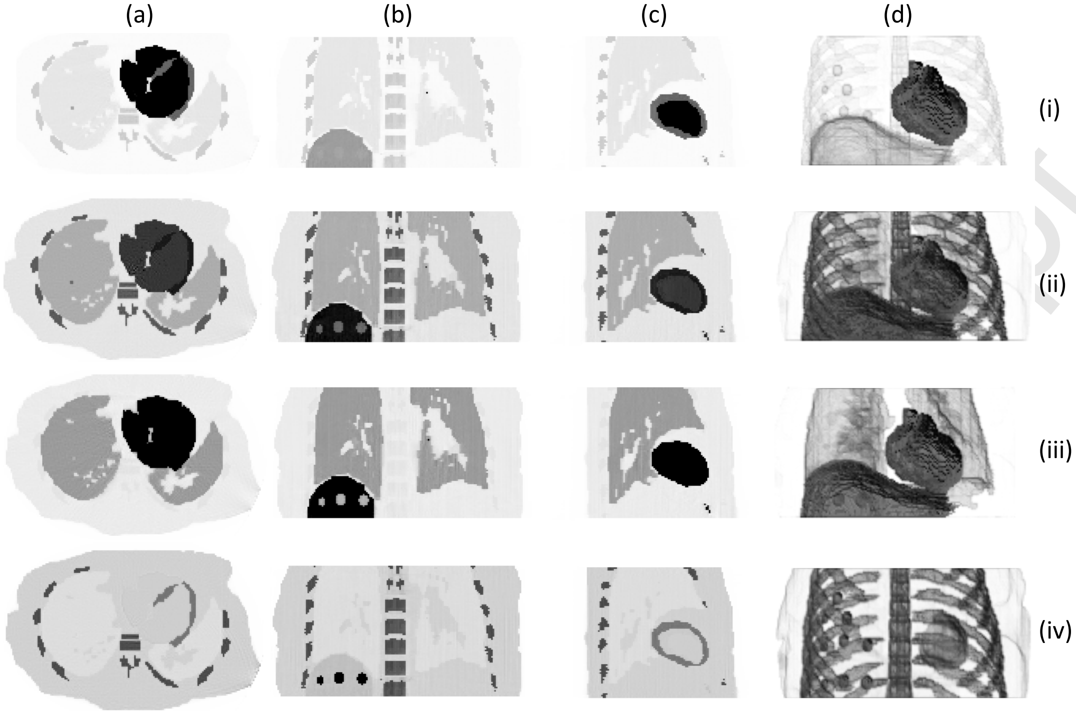

Fig. 7. Transverse (a), coronal (b), sagittal (c) and 3D rendered (d) reconstructed [^{15}O]H$_2$O (i-ii) and [^{18}F]FDG (iii-iv) emission images at 2 different time points corresponding to an early time frame (i, iii) and a late time frame (ii,iv) where t_0 is the reference start time. Images are shown for a single respiratory gate corresponding to motionless data.

excluded to accommodate simulation of different breathing patterns. Using all 8 gates, increased motion is simulated in the superior-inferior direction since the bulk of the motion occurs in this direction. During end-inspiration the lungs covered 359802 mm^3 while during end expiration a ~23% difference in volume was observed with the lungs covering 283954 mm^3. Similarly in Fig. 6, an early and late [^{18}F]FDG time frame is shown for a single gate and for all gates superimposed. As seen from the coronal images (Fig. 6b), the irreversible trapping of the tracer in the tumors is evident with increased activity concentration in the late frame signifying increased uptake rate. Motionless projection data from the reference gate were reconstructed as described in the methods Section. Reconstructed images from both the dynamic [^{15}O]H$_2$O (i-ii) and [^{18}F]FDG (iii-iv) studies are displayed in Fig. 7. The images representing again an early and a late time frame correspond to those from the motionless dynamic phantoms shown in Figs. 5 and 6. The reconstructed images are qualitatively identical to the simulated ones, demonstrating the capabilities of this parametric phantom in algorithmic development for image reconstruction applications. However, in parametric imaging studies, the endpoint parameters are the micro- or macro-parameter maps, rather than images of activity concentration. As such and following image reconstruction, full kinetic analysis was performed on the dynamic datasets for both studies.

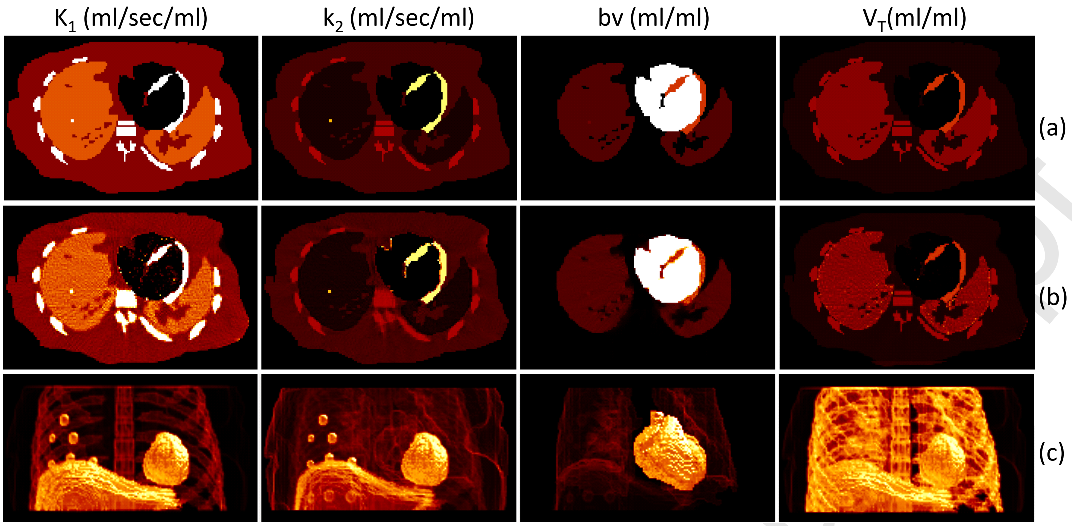

Fig. 8. Parametric images of K_1, k_2, bv and V_T (a) simulated and (b) estimated (using GLLS) following 3D reconstruction of the simulated single gate dynamic [^{15}O]H_2O phantom dataset. Rendered images of the estimated maps are also shown in (c).

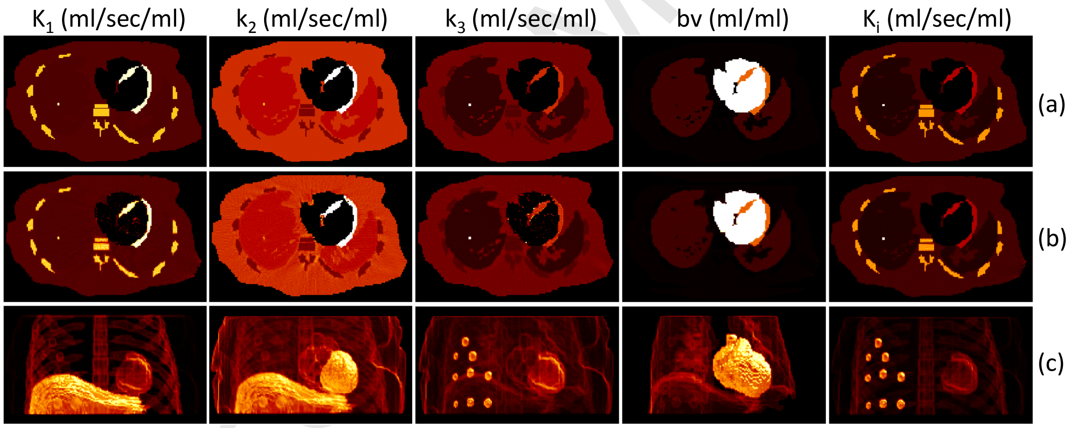

Fig. 9. Parametric images of K_1, k_2, k_3, bv and K_i, (a) simulated and (b) estimated (using GLLS), following 3D reconstruction of the simulated single gate dynamic [^{18}F]FDG phantom dataset. Rendered images of the estimated maps are also shown in (c).

Fig. 8 shows the simulated parametric images of influx rate (K_1), efflux rate (k_2), blood volume (bv) and volume of distribution (V_T) as well as the estimated parametric maps following post-reconstruction kinetic analysis of the dynamic [^{15}O]H_2O dataset. 3D rendered images of the estimated parametric maps are also shown. Similarly, Fig. 9 displays the simulated K_1, k_2, k_3, bv and K_i parametric images and the estimated transverse and 3D rendered parametric maps following post-reconstruction kinetic analysis of the dynamic [^{18}F]FDG dataset. As can be seen in both studies, there is a good differentiation between the tissue and the blood components. The estimated

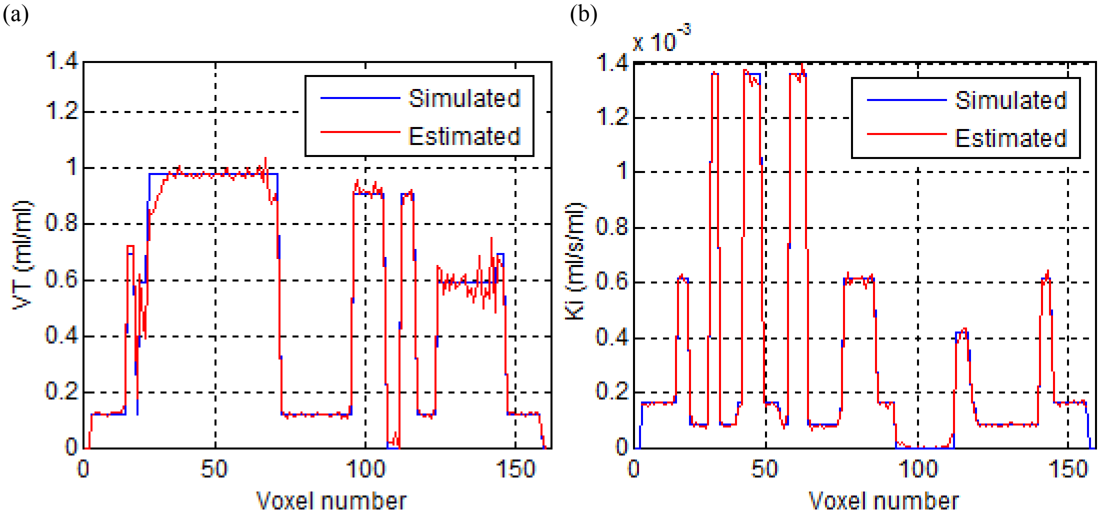

Fig. 10 Profiles through (a) the volume of distribution (V_T) and (b) net uptake rate (K_i) parametric images, obtained from the dynamic [^{15}O]H$_2$O and [^{18}F]FDG datasets respectively. Profiles are shown for the simulated and the estimated parameters following post-reconstruction kinetic analysis.

parametric maps appear broadly similar to the simulated ones while both micro- and macro-parameter maps can be estimated with the proposed simulation platform. Again since projections from a single gate were used, the estimated parametric maps are representative of motionless data. Consequently, any visible blurring in the estimated parametric maps is attributed to the lack of convergence during image reconstruction. A more quantitative comparison can be seen in Fig.10 where profiles through the V_T and K_i parametric images from the [^{15}O]H$_2$O and [^{18}F]FDG dataset are plotted. Reconstructed V_T values vary between 0 and 1 ml/ml depending on the region while K_i, representing the net uptake rate, vary between 0 and 0.00133 ml/s/ml with the maximum net uptake seen in the tumors.

V. DISCUSSION

A 5D anthropomorphic computational phantom for parametric imaging studies in dynamic emission tomography based on a generic simulation platform is described. The new platform comprises of a patient specific MR-segmented anatomical representation, including user-defined patient specific anatomical variants, coupled with a detailed kinetic modelling simulator, capable of generating realistic dynamic imaging protocols based on any given tracer specific model. The phantom is envisaged to become available for academic research applications in imaging physics, providing a library of anatomical phantoms coupled with the pharmacokinetic simulator and representative motion fields. Supplementary models, in addition to those demonstrated in this study could be incorporated along with additional functionality.

Compared to current computational phantoms reported in the literature, such as the NCAT and XCAT [10], the proposed design lacks the flexibility offered by coupling mathematical models to detailed generalized anatomical information. However, the proposed methodology counterbalances this by benefiting from a fast simulation environment, with semi-automatic segmentation techniques, making it possible to simulate personalized dynamic protocols [39]. Having the MR data available, construction of the anatomical phantom, kinetic modelling simulation, motion field estimation and application, and forward projection to generate the raw emission and attenuation data should take between 20 and 25 hours [15]. However the majotiy of this time is taken by the forward projection step and depends on the imaging system, the number of respiratory gates and the kinetic modelling framing being simulated. With the recent advent of hybrid PET-MR systems, MR information is readily available for each patient, omitting the need for additional scanning sessions [40]. Furthermore, MR offers a competitive advantage compared to CT-derived anatomical phantoms since it results in no radiation dose to the subject. However, if other patient-specific anatomical information is available from different modalities, this can easily be incorporated to picture a more detailed anatomical representation. However, in this case, the additional structural information would need to be registered to the MR space prior to being segmented and incorporated in the phantom. If MR information is not available and the anatomical information derived exclusively from a different modality (such as CT), then there is no need for additional registration as the structural information is derived solely from a single modality. While patient-specific models can be realized, in cases where only a generic anatomical representation is needed, template anatomical information can be drawn from an anatomical library based on databases of healthy males and females.

Apart from a more personalized anatomical design, the dynamic phantom in reference paves the way for generic realistic parametric imaging simulation studies not previously available with application-specific platforms such as PCAT [23]. For algorithmic development, kinetic parameters for all organ structures can be drawn from existing literature; however, again if a more personalized simulation is needed, following kinetic analysis of an existing dynamic study, patient-specific kinetic parameters can be used in conjunction with the tracer-specific model and a patient or population based input function.

One of the drawbacks of voxelized phantoms, previously seen as a disadvantage compared to mathematical and hybrid phantoms is their inability to describe periodical motion induced variations [10]. However, this drawback was overcame by exploiting the possibility to transform the dynamic PET data with MR-derived motion fields and to generate a number of PET gates, simulating realistic respiratory motion within each time frame in the dynamic imaging protocol. One of the benefits of such an approach, amongst others, is the ability to provide a platform to investigate and develop a number of kinetic modelling related methods and techniques in the presence of motion.

Although the current phantom significantly enhances the simulation capabilities in the field of parametric imaging in emission tomography, further improvements can be accommodated. Extension of the simulated FOV from a single bed position to a multi-bed coverage is achievable since current PET-MR systems perform whole body acquisition protocols. This is of particular relevance since whole-body parametric imaging protocols have recently been introduced, demonstrating enhanced tumor detectability and more accurate quantification compared to traditional static imaging protocols relying on SUV indices [41].

Apart from improvements in the anatomy, further improvements can be realized in simulating the transit of the tracer through the vasculature and capillaries following tracer injection. More detailed modelling of the underlying physiological processes governing the tracer's delivery and uptake can further enhance the simulation capabilities of the existing platform, especially for drug and tracer development studies. Two PET dynamic protocols were demonstrated in this work, representing the bulk of imaging applications in PET imaging. The platform can also be used in a similar way for any clinical application in SPECT imaging. Furthermore, even though the platform is primarily designed for parametric imaging studies in emission tomography, it can easily be extended to accommodate dynamic simulation studies for other modalities. Dynamic contrast enhanced MRI and CT using iodine-based contrast agents can take advantage of the proposed methodology to investigate different pharmacokinetic related methods and techniques [42]. Although kinetic modelling in these modalities is slightly different compared to emission tomography techniques [43], the software can easily be extended in the future to incorporate pharmacokinetic models tailored to DCE-MR and DCE-CT imaging protocols.

VI. CONCLUSION

As dynamic imaging protocols are adopted more frequently for clinical research and drug development, simulation solutions for more efficient development, evaluation and validation of novel tracers, protocols, methods and techniques in parametric imaging studies, are of interest. In this work, a new 5D computational phantom for generating realistic datasets for parametric imaging studies in emission tomography, was presented. The proposed phantom can be used for a number of applications both in PET and SPECT, including motion tracking and correction, conventional and direct image reconstruction algorithm development, dynamic imaging protocol design, simulations for tracer and drug development and kinetic parameter estimation algorithm development. As such, the phantom and software platform will be a valuable tool for the molecular imaging community and is envisaged to become available for simulation studies in dynamic tomography.

ACKNOWLEDGMENTS

This work was supported by the Swiss National Science Foundation under grants SNSF 31003A-135176 and 31003A-149957 as well as EU COST Action TD1007 (www.pet-mri.eu). Data to become available at http://www.isd.kcl.ac.uk/pet-mri/simulated-data/.

Conflict of Interest statement

The authors declare that they have no conflict of interest.

REFERENCES

[1] Zaidi H, Tsui BMW. Review of computational anthropomorphic anatomical and physiological models. Proceedings of the IEEE. 2009;97:1938-53.

[2] Shepp LA, Logan BF. The Fourier reconstruction of a head section. IEEE Trans Nucl Sci. 1974;21:21-43.

[3] Segars WP, Lalush DS, Tsui BMW. Modeling respiratory mechanics in the MCAT and spline-based MCAT phantoms. IEEE Trans Nucl Sci. 2001;48:89-97.

[4] Tsoumpas C, Gaitanis A. Modeling and Simulation of 4D PET-CT and PET-MR Images. PET Clinics. 2013;8:95-110.

[5] Zubal IG, Harrell CR, Smith EO, Rattner Z, Gindi G, Hoffer PB. Computerized three-dimensional segmented human anatomy. Med Phys. 1994;21:299-302.

[6] Hoffman EJ, Cutler PD, Digby WM, Mazziotta JC. 3-D phantom to simulate cerebral blood flow and metabolic images for PET. IEEE Trans Nucl Sci. 1990;37:616-20.

[7] Xu XG, Chao TC, Bozkurt A. VIP-Man: an image-based whole-body adult male model constructed from color photographs of the Visible Human Project for multi-particle Monte Carlo calculations. Health Phys. 2000;78:476-86.

[8] Dimbylow P. Development of the female voxel phantom, NAOMI, and its application to calculations of induced current densities and electric fields from applied low frequency magnetic and electric fields. Phys Med Biol. 2005;50:1047-70.

[9] Nipper JC, Williams JL, Bolch WE. Creation of two tomographic voxel models of paediatric patients in the first year of life. Phys Med Biol. 2002;47:3143-64.

[10] Segars WP, Tsui BMW. MCAT to XCAT: The evolution of 4D computerized phantoms for imaging research. Proceedings of the IEEE. 2009;97:1954-68.

[11] Segars WP. Development and application of the new dynamic NURBS-based cardiac-torso (NCAT) phantom [PhD Thesis]: University of North Carolina, Chapel Hill, NC, USA; 2001.

[12] Segars WP, Mori S, Chen GTY, Tsui BMW. Modeling respiratory motion variations in the 4D NCAT phantom. Conference Record IEEE Nuclear Science Symposium. 2007; p. 2677-9.

[13] Segars WP, Sturgeon G, Mendonca S, Grimes J, Tsui BM. 4D XCAT phantom for multimodality imaging research. Med Phys. 2010;37:4902-15.

[14] Konik A, Connolly CM, Johnson KL, Dasari P, Segars P, Hendrik Pretorius P, et al. Digital anthropomorphic phantoms of non-rigid human respiratory and voluntary body motions: A tool-set for investigating motion correction in 3D reconstruction. IEEE Nuclear Science Symposium and Medical Imaging Conference (NSS/MIC), 2011. p. 3572-8.

[15] Tsoumpas C, Buerger C, King AP, Mollet P, Keereman V, Vandenberghe S, et al. Fast generation of 4D PET-MR data from real dynamic MR acquisitions. Phys Med Biol. 2011;56:6597–613.

[16] Aboagye EO. Imaging in drug development. Clin Adv Hematol Oncol. 2006;4:902-4.

[17] Takesh M. The Potential Benefit by Application of Kinetic Analysis of PET in the Clinical Oncology. ISRN oncology. 2012;2012:349351.

[18] Reader AJ, Matthews JC, Sureau FC, Comtat C, Trebossen R, Buvat I. Iterative Kinetic Parameter Estimation within Fully 4D PET Image Reconstruction. Conference Record IEEE Nuclear Science Symposium, 2006. p. 1752-6.

[19] Tong S, Alessio AM, Kinahan PE, Liu H, Shi P. A robust state-space kinetics-guided framework for dynamic PET image reconstruction. Phys Med Biol. 2011;56:2481-98.

[20] Verhaeghe J, D'Asseler Y, Vandenberghe S, Staelens S, Van De Walle R, Lemahieu I. ML reconstruction from dynamic list-mode PET data using temporal splines. Conference Record IEEE Nuclear Science Symposium, 2004. Vol. 5, p. 3146-50.

[21] Wernick MN, Infusino EJ, Milosevic M. Fast spatio-temporal image reconstruction for dynamic PET. IEEE Trans Med Imaging. 1999;18:185-95.

[22] Li Q, Asma E, Ahn S, Leahy RM. A fast fully 4-D incremental gradient reconstruction algorithm for list mode PET data. IEEE Trans Med Imaging. 2007;26:58-67.

[23] Fung GSK, Higuchi T, Park MJ, Segars WP, Tsui BMW. Development of a 4D digital phantom for tracer kinetic modeling and analysis of dynamic perfusion PET and SPECT simulation studies. IEEE Nuclear Science Symposium and Medical Imaging Conference (NSS/MIC), 2011. p. 4192-5.

[24] Tsoumpas C, Polycarpou I, Thielemans K, Buerger C, King AP, Schaeffter T, et al. The effect of regularization in motion compensated PET image reconstruction: a realistic numerical 4D simulation study. Phys Med Biol. 2013;58:1759-73.

[25] Buerger C, Tsoumpas C, Aitken A, King AP, Schleyer P, Schulz V, et al. Investigation of MR-Based Attenuation Correction and Motion Compensation for Hybrid PET/MR. IEEE Trans Nucl Sc. 2012;59:1967-76.

[26] Renkin EM. Transport of potassium-42 from blood to tissue in isolated mammalian skeletal muscles. Am J Physiol. 1959;197:1205-10.

[27] Crone C. The permeability of capillaries in various organs as determined by use of the indicator diffusion method. Acta Physiol Scand. 1963;58:292-305.

[28] Kety SS. The theory and applications of the exchange of inert gas at the lungs and tissues. Pharmacol Rev. 1951;3:1-41.

[29] Kudomi N, Slimani L, Jarvisalo MJ, Kiss J, Lautamaki R, Naum GA, et al. Non-invasive estimation of hepatic blood perfusion from H2 15O PET images using tissue-derived arterial and portal input functions. Eur J Nucl Med Mol Imaging. 2008;35:1899-911.

[30] Ludemann L, Sreenivasa G, Michel R, Rosner C, Plotkin M, Felix R, et al. Corrections of arterial input function for dynamic H215O PET to assess perfusion of pelvic tumours: arterial blood sampling versus image extraction. Phys Med Biol. 2006;51:2883-900.

[31] Peters J, Ecabert O, Meyer C, Kneser R, Weese J. Optimizing boundary detection via Simulated Search with applications to multi-modal heart segmentation. Med Imag Anal. 2010;14:70-84.

[32] Lodge MA, Carson RE, Carrasquillo JA, Whatley M, Libutti SK, Bacharach SL. Parametric images of blood flow in oncology PET studies using [15O]water. J Nucl Med. 2000;41:1784-92.

[33] Wienhard K. Measurement of glucose consumption using [(18)F]fluorodeoxyglucose. Methods 2002;27:218-25.

[34] Buerger C, Schaeffter T, King AP. Hierarchical adaptive local affine registration for fast and robust respiratory motion estimation. Med Imag Anal. 2011;15:551-64.

[35] Brambilla M, Secco C, Dominietto M, Matheoud R, Sacchetti G, Inglese E. Performance characteristics obtained for a new 3-dimensional lutetium oxyorthosilicate-based whole-body PET/CT scanner with the National Electrical Manufacturers Association NU 2-2001 standard. J Nucl Med. 2005;46:2083-91.

[36] Kotasidis FA, Matthews JC, Angelis GI, Noonan PJ, Jackson A, Price P, et al. Single scan parameterization of space-variant point spread functions in image space via a printed array: the impact for two PET/CT scanners. Phys Med Biol. 2011;56:2917-42.

[37] Dagan F, Huang SC, ZhiZhong W, Dino H. An unbiased parametric imaging algorithm for nonuniformly sampled biomedical system parameter estimation. IEEE Trans Med Imaging. 1996;15:512-8.

[38] Feng D, Ho D, Lau KK, Siu WC. GLLS for optimally sampled continuous dynamic system modeling: theory and algorithm. Comput Methods Programs Biomed. 1999;59:31-43.

[39] Stute S, Vauclin S, Necib H, Grotus N, Tylski P, Rehfeld NS, et al. Realistic and Efficient Modeling of Radiotracer Heterogeneity in Monte Carlo Simulations of PET Images With Tumors. IEEE Trans Nucl Sci. 2012;59:113-22.

[40] Zaidi H, Ojha N, Morich M, Griesmer J, Hu Z, Maniawski P, et al. Design and performance evaluation of a whole-body Ingenuity TF PET-MRI system. Phys Med Biol. 2011;56:3091-106.

[41] Karakatsanis NA, Lodge MA, Yun Z, Mhlanga J, Chaudhry MA, Tahari AK, et al. Dynamic multi-bed FDG PET imaging: Feasibility and optimization. IEEE Nuclear Science Symposium and Medical Imaging Conference (NSS/MIC) 2011. p. 3863-70.

[42] Ingrisch M, Sourbron S. Tracer-kinetic modeling of dynamic contrast-enhanced MRI and CT: a primer. J Pharmacokinet Pharmacodyn. 2013;40:281-300.

[43] Sourbron SP, Buckley DL. Classic models for dynamic contrast-enhanced MRI. NMR Biomed. 2013; 26:1004-1027.

List of Tables

TABLE I

SIMULATED KINETIC PARAMETER FOR THE SINGLE-TISSUE MODEL

	K_1 ml/s/ml	k_2 ml/s/ml	Bv ml/ml	VT ml/ml
Lungs	0.0008	0.0014	0.06	0.6
Bone	0.0018	0.0027	0.00	0.69
Soft tissue	0.0005	0.0042	0.00	0.12
Ventricles	0.0000	0.0000	1.00	0.00
Myocardium	0.0167	0.0183	0.15	0.91
Tumors	0.0098	0.0161	0.08	0.61
Liver	0.0117	0.0119	0.05	0.98

TABLE II

SIMULATED KINETIC PARAMETER FOR THE TWO-TISSUE MODEL

	K_1 ml/s/ml	k_2 ml/s/ml	k_3 ml/s/ml	Bv ml/ml	K_i ml/s/ml
Lungs	0.0007	0.0048	0.0006	0.1510	0.0001
Bone	0.0027	0.0033	0.0010	0.0000	0.0006
Soft tissue	0.0008	0.0054	0.0014	0.0190	0.0002
Ventricles	0.0000	0.0000	0.0000	1.0000	0.0000
Myocardium	0.0033	0.0170	0.0025	0.5450	0.0004
Tumors	0.0031	0.0073	0.0056	0.0800	0.0014
Liver	0.0209	0.0222	0.0000	0.1650	0.0000

List of Figures

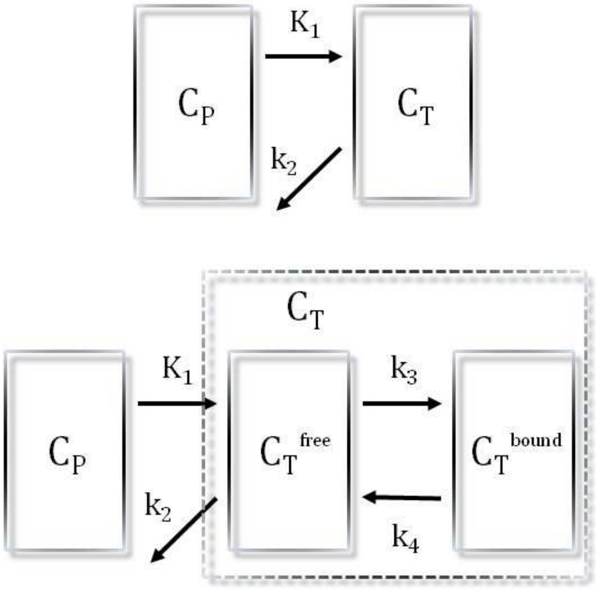

Fig. 1. Schematic diagram of a single-tissue (top) and a two-tissue (bottom) kinetic models showing the different compartments as well as the constant rate controlling the rate of change in activity concentration for each compartment.

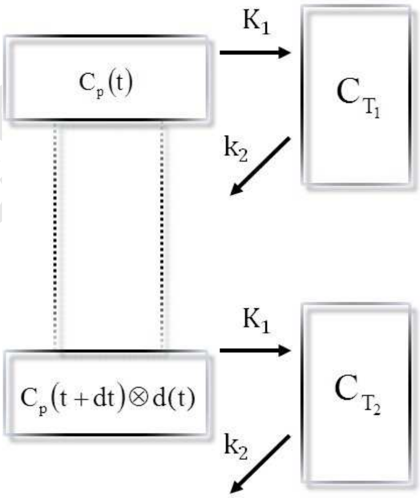

Fig. 2. Schematic diagram of a single-tissue model at 2 different target regions. As the injected bolus passes through the blood stream it becomes dispersed while its arrival time is shifted. The option to use different delay and dispersion parameters for each organ in the phantoms improves the level of realism compared to using a common delay and dispersion for the entire phantom.

Fig. 3. Transverse (a), coronal (b) and sagittal (c) images of the simulated attenuation map corresponding to a single gate.

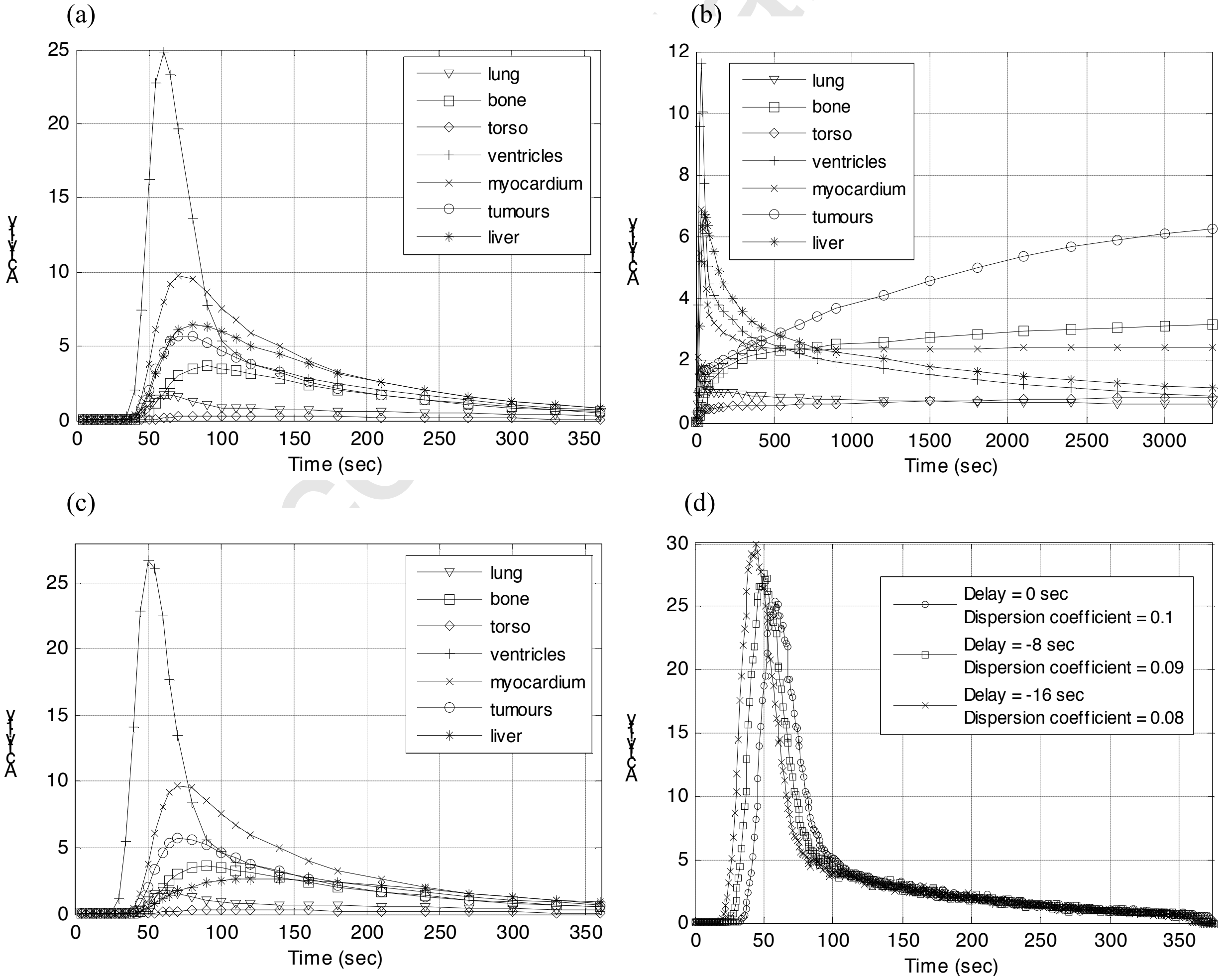

Fig. 4. Simulated TACs representing (a) [^{15}O]H_2O and (b) [^{18}F]FDG kinetics, used for the different regions of interest in the 3D anatomical phantom. Input functions with differential delay and dispersion in different organs can be used while organ TACs having a dual input function delivery can also be simulated. The simulated [^{15}O]H_2O TACs from (a) are shown in (c) using a dual input model in the liver, while 3 input functions from a [^{15}O]H_2O scan with different delay and dispersion are shown in (d).

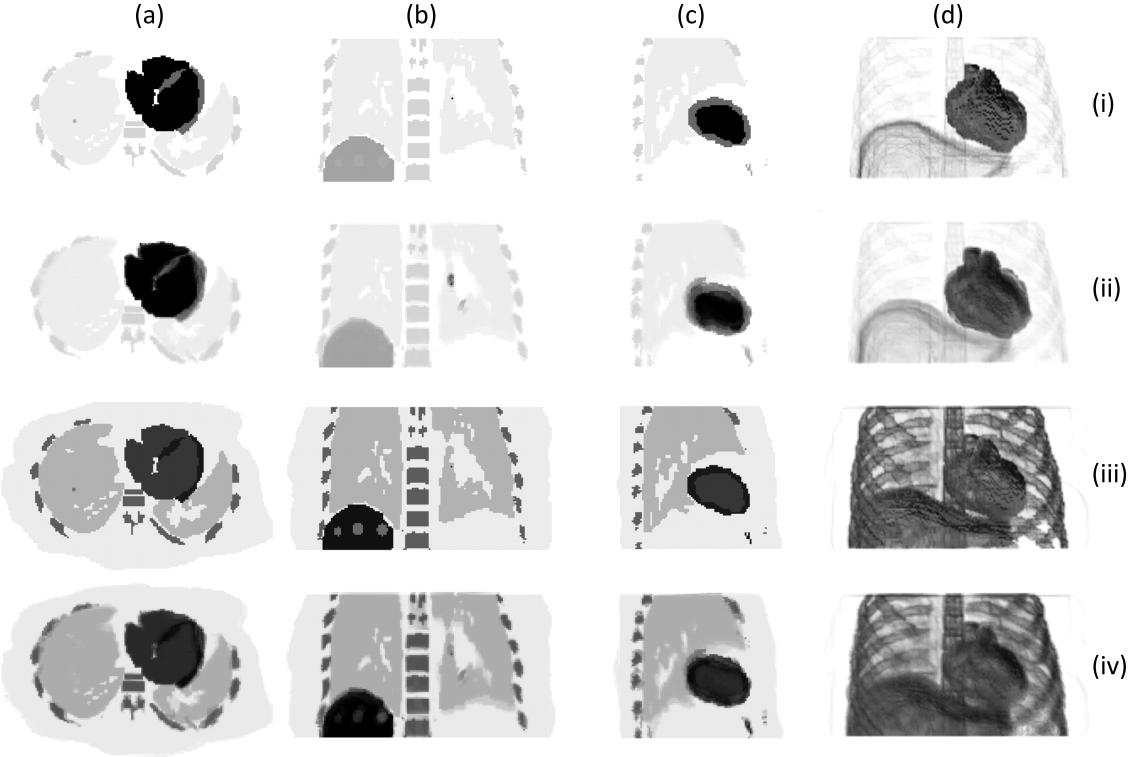

Fig. 5. Transverse (a), coronal (b), sagittal (c) and 3D rendered (d) simulated images of the [^{15}O]H_2O phantom at 2 different time points during the simulated dynamic [^{15}O]H_2O image sequence corresponding to an early time frame (i-ii) ($t = t_0 + 20$ s) and a late time frame (iii-iv) ($t = t_0 + 360$ s) where t_0 is the reference start time. Images are shown for a single respiratory gate corresponding to motionless data (i, iii) and for all gates superimposed and corresponding to motion affected data (ii, iv).

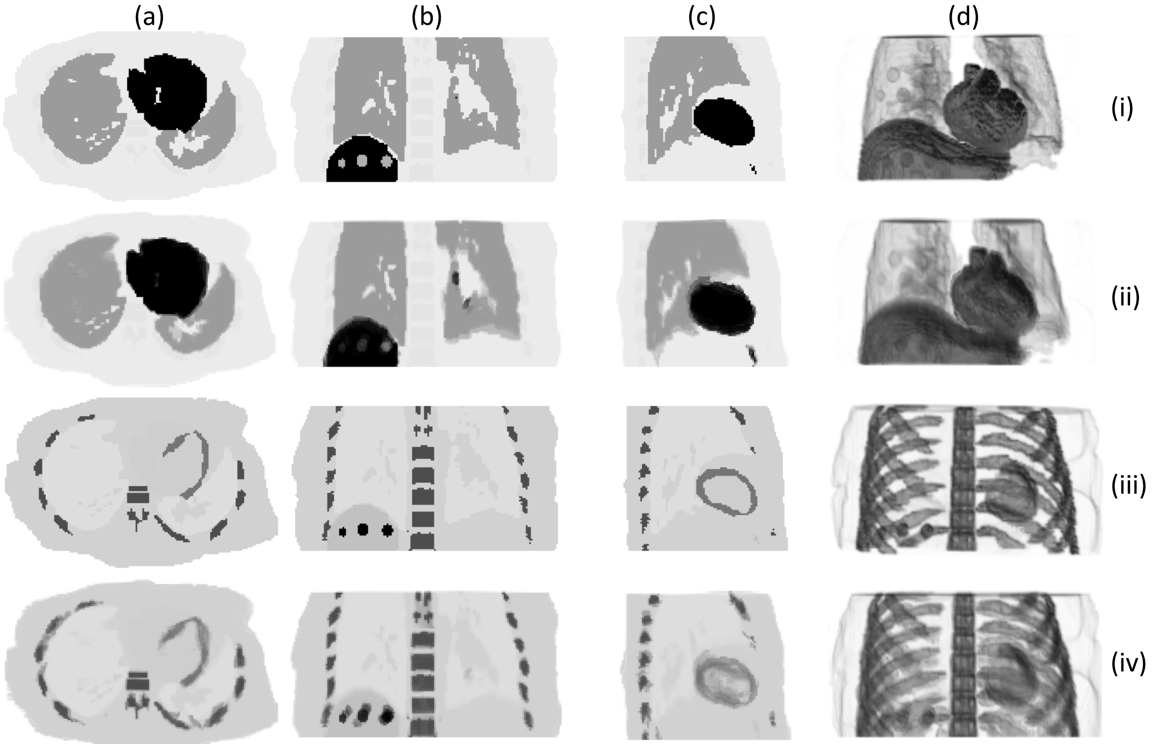

Fig. 6. Transverse (a), coronal (b), sagittal (c) and 3D rendered (d) simulated images of the [^{18}F]FDG phantom at 2 different time points during the simulated dynamic [^{18}F]FDG image sequence corresponding to an early time frame (i-ii) ($t = t_0 + 40$ s) and a late time frame (iii-iv) ($t = t_0 + 3400$ s) where t_0 is the reference start time. Images are shown for a single respiratory gate corresponding to motionless data (i, iii) and for all gates superimposed and corresponding to motion affected data (ii, iv).

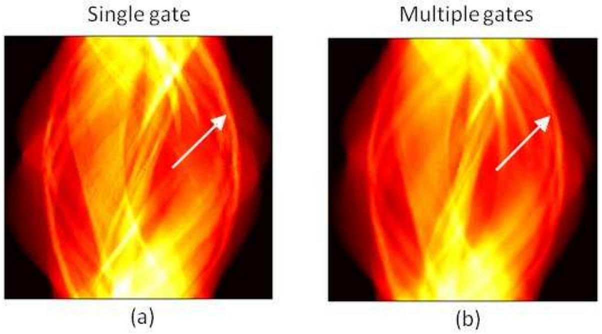

Fig. 7. Representative sinograms after forward projecting the dynamic 5D phantom. Projection data are shown at a late time frame from a single gate, simulating a motion free dataset (a) and from an average sinogram after combining all gates, simulating a motion affected dataset (b).

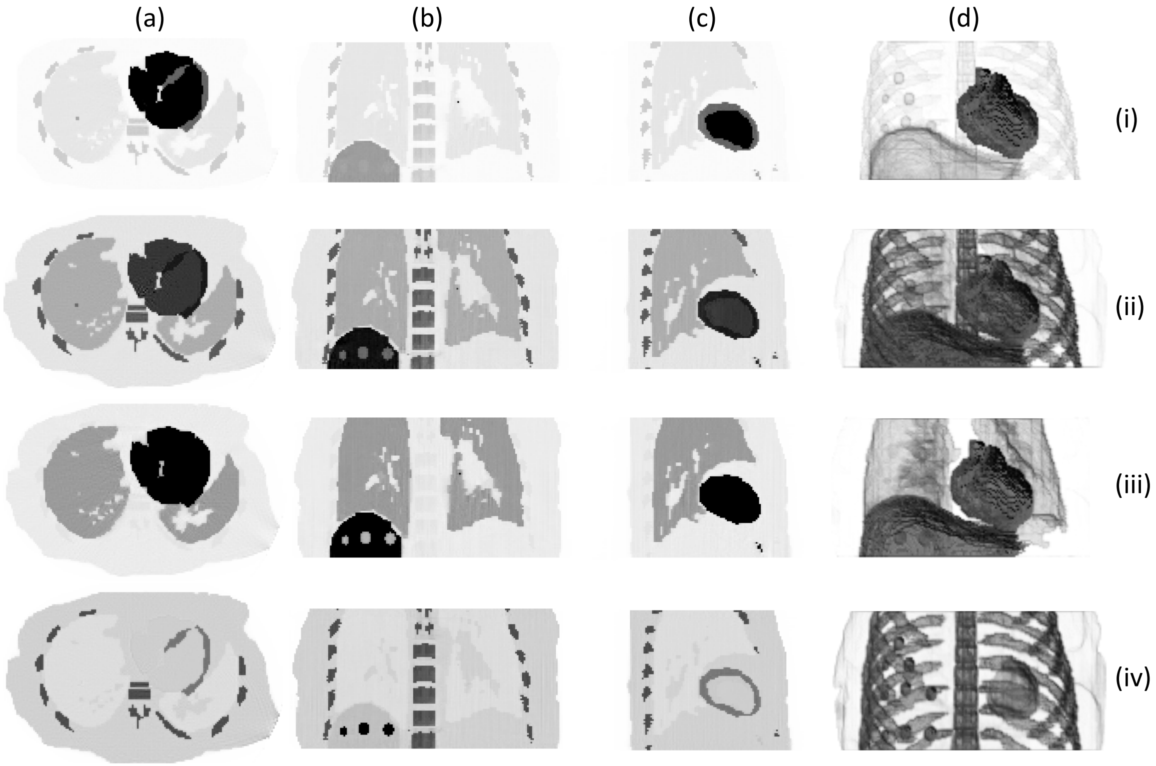

Fig. 8. Transverse (a), coronal (b), sagittal (c) and 3D rendered (d) reconstructed [^{15}O]H_2O (i-ii) and [^{18}F]FDG (iii-iv) emission images at 2 different time points corresponding to an early time frame (i, iii) and a late time frame (ii,iv) where t_0 is the reference start time. Images are shown for a single respiratory gate corresponding to motionless data.

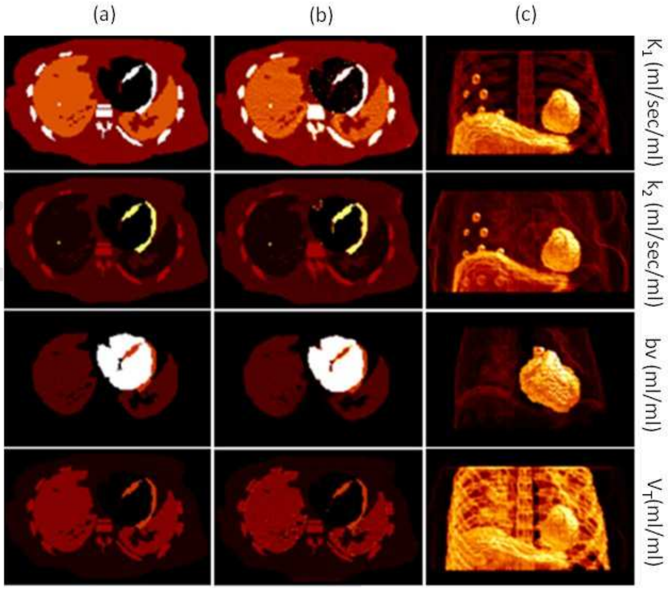

Fig. 9. Parametric images of K_1, k_2, bv and V_T (a) simulated and (b) estimated (using GLLS) following 3D reconstruction of the simulated single gate dynamic [^{15}O]H_2O phantom dataset. Rendered images of the estimated maps are also shown in (c).

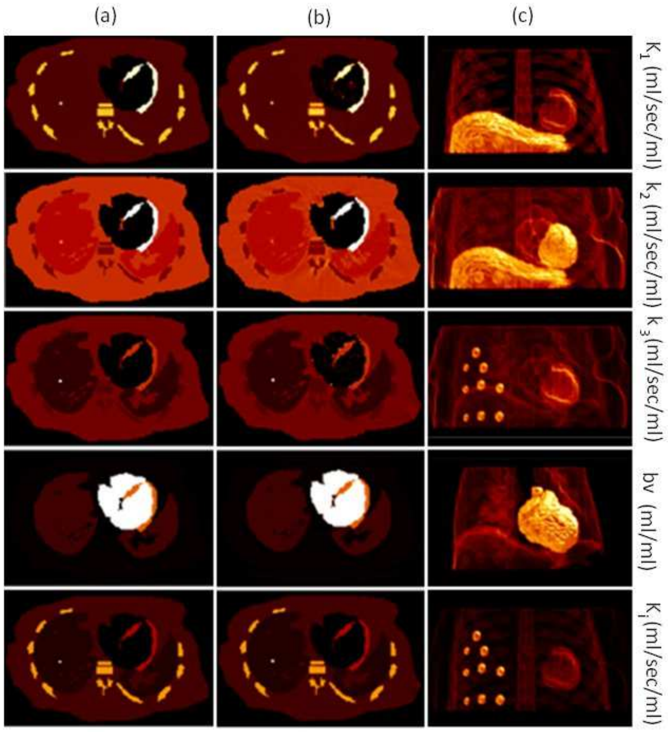

Fig. 10. Parametric images of K_1, k_2, k_3, bv and $K_{i,}$ (a) simulated and (b) estimated (using GLLS), following 3D reconstruction of the simulated single gate dynamic [^{18}F]FDG phantom dataset. Rendered images of the estimated maps are also shown in (c).

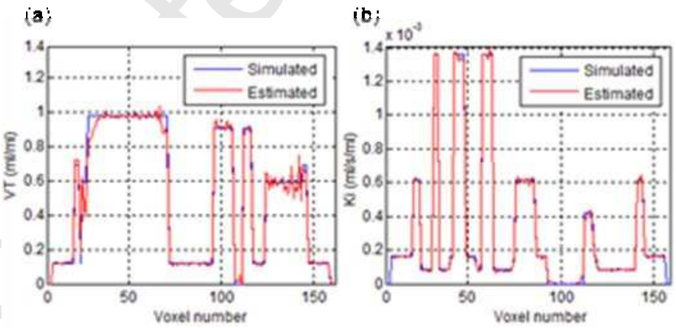

Fig. 11 Profiles through (a) the volume of distribution (V_T) and (b) net uptake rate (K_i) parametric images, obtained from the dynamic [^{15}O]H_2O and [^{18}F]FDG datasets respectively. Profiles are shown for the simulated and the estimated parameters following post-reconstruction kinetic analysis.

Highlights

- Dynamic image acquisition protocols are increasingly used in emission tomography
- Need for computational phantoms to describe both the spatial and temporal distribution of radiotracers.
- A 5D anthropomorphic phantom was developed, for parametric imaging simulations in emission tomography.
- The phantom is based on real 4D MR data and a detailed multi-compartmental pharmacokinetic modelling simulator.
- Example applications are shown in parametric [^{18}F]FDG and [^{15}O]H_2O PET imaging.